Structure Analysis of Amyloid Aggregates at Lipid Bilayers by Supercritical Angle Raman Microscopy

Dubois, Valentin ; Serrano, Diana ; Zhang, Xiaotian ; Seeger, Stefan

Abstract: The amyloid- peptide is correlated with Alzheimer's disease and is assumed to cause toxicity by its interaction with the neuron membrane. A custom-made microscope objective based on the supercritical angle technique was developed by our group, which allows investigation of interfacial events by performing surface-sensitive and low-invasive spectroscopy. Applied to Raman spectroscopy, this technique was used to collect information about the structure of polypeptides that interact with a supported lipid bilayer. Notably, the conformation used by amyloid- (1–40) and amyloid- (1–42) when interacting directly with or next to the supported lipid bilayer was characterized. We observed two distinct secondary structures, -helix and -sheet, which were exhibited by the peptide. These two structures were detected simultaneously. The propensity of the peptide to fold into these structures seemed dependent on both their number of amino acids and their proximity with the supported lipid bilayer. The -helix structure was observed for amyloid- (1–42) fragments that were closer to the lipid bilayer. Peptides that were located further away from the bilayer favored the -sheet structure. Amyloid- (1–40) was less prone to adopt the -helix secondary structure.

DOI: https://doi.org/10.1021/acs.analchem.9b05092

Originally published at:
Dubois, Valentin; Serrano, Diana; Zhang, Xiaotian; Seeger, Stefan (2020). Structure Analysis of Amyloid Aggregates at Lipid Bilayers by Supercritical Angle Raman Microscopy. Analytical Chemistry, 92(7):4963-4970.
DOI: https://doi.org/10.1021/acs.analchem.9b05092

Structure Analysis of amyloid aggregates at lipid bilayers by Supercritical Angle Raman Microscopy.

Valentin Dubois, Diana Serrano, Xiaotian Zhang and Stefan Seeger*.

Department of Chemistry, University of Zürich, Winterthurerstrasse 190, CH-8057 Zürich, Switzerland.

ABSTRACT: The amyloid-β peptide is correlated with Alzheimer's disease and is assumed to cause toxicity by its interaction with the neuron membrane. A custom-made microscope objective based on the supercritical angle technique was developed by our group, which allows investigation of interfacial events by performing surface-sensitive and low-invasive spectroscopy. Applied to Raman spectroscopy, this technique was used to collect information about the structure of polypeptides that interact with a supported lipid bilayer. Notably, the conformation used by amyloid-β(1–40) and amyloid-β(1–42) when interacting directly with or next to the supported lipid bilayer was characterized. We observed two distinct secondary structures, α-helix and β-sheet, which were exhibited by the peptide. These two structures were detected simultaneously. The propensity of the peptide to fold into these structures seemed dependent on both their number of amino acids and their proximity with the supported lipid bilayer. The α-helix structure was observed for amyloid-β(1–42) fragments that were closer to the lipid bilayer. Peptides that were located further away from the bilayer favored the β-sheet structure. Amyloid-β(1–40) was less prone to adopt the α-helix secondary structure.

Proteins and polypeptide chains are major actors in biochemistry. Their functions are intrinsically based on their amino acid sequence and their three-dimensional structure, which exhibit the proper chemical groups and/or environment for specific biological reactions. Their structure, which is also called their conformation, is stabilized by numerous non-covalent interactions between the amino acids of the peptide chain[1,2]. After synthesis of the molecule in vivo, its conformation is reached in a short time frame by the gathering of smaller local structures, called secondary structures. The most important secondary structures are called α-helix and β-sheet. However, incorrect conformations can be formed, which are stable enough so that restructuring toward the correct functional structure does not occur[3]. These "misfolded" polypeptides are likely to promote health problems by canceling the necessary biological functions or gaining toxic properties[4,5]. Some of these polypeptides are known to be prone to misfolding and are recognized as the main cause of various diseases, such as Alzheimer's[6,7], Parkinson's[8–10], or type 2 diabetes[11]. For example, Alzheimer's disease is a neurodegenerative disease of particular interest that has characteristic extracellular deposition of aggregated amyloid-β peptides (Aβ) as a plaque surrounding the neurons[7]. Aβ is a small peptide that is produced from the cleavage of a transmembrane protein called amyloid-β precursor protein (APP). Aβ fragments can have different sizes depending on the number of remaining amino acids after APP cleavage. However, the most common Aβ peptides in Alzheimer's plaque have 40 or 42 amino acids[12,13]. The native structure of Aβ is usually described either as a random coil in aqueous solution[14] or as a small α-helix when interacting with membrane or hydrophobic surfaces[15,16]. Upon aggregation, this peptide exhibits a specific structure that is known as amyloid fibril, which consists of a stack of β-sheets perpendicular to the fibril axis[17,18]. The cause of its toxicity toward neurons remains unclear. Different effects have been observed following peptide aggregation, which could justify the neuronal death encountered in the brain of disease patients. These effects include oxidation of lipid molecules in neuron membranes [19,20], lipid mobility hindrance within the bilayer[21], and pore-like channel formation through the cell membrane[22–24]. Different in vitro lipid structures have been established to study their interaction with peptides, assuming that the behavior of these models can be partially extrapolated to a real neuron membrane in vivo[25,26]. Among these models, supported lipid bilayers (SLBs) are planar fluid membranes that are formed by deposition and fusion of unilamellar vesicles (ULVs) onto hydrophilic substrate[27]. A SLB is easy to form on a support and it is attractive because of its simplicity. It also forms directly on an interface between the support and the sample medium. This last feature makes the SLBs particularly suitable for surface-sensitive techniques because the interaction with peptides will occur only within this interfacial region. Supercritical angle spectroscopy is one of these surface-selective techniques. It allows differentiation between species that emit a signal from the interface and those that protrude above the interface or diffuse in the bulk solution, without a washing step to remove unbound molecules. The capability to observe processes at, and close to, the surface simultaneously allows high precision kinetic studies to be performed and axial resolution of molecule localization down to 1 nm. This is achieved by collecting the photons above the angle of total internal reflection (critical angle) at a glass–water interface. Molecules that are situated near such an interface between two media of different refractive indexes that emit a significant part of their radiation above the corresponding critical angle (supercritical light). This portion of the signal decreases exponentially with the axial distance between the emitters and the interface. A specific collection of the signal above the critical angle typically excludes the signal that is emitted beyond a range of approximately 200 nm from the interface, with a detection efficiency that decreases exponentially[28,29]. In addi-

tion, the undercritical angle signal can be collected simultaneously. The latter collection corresponds to the output of a traditional confocal microscope. It allows detection of photons emitted above the interface with a collection efficiency that extends up to ~2.5 µm on the axial axis[30]. Supercritical angle spectroscopy has been used to study the interaction between a negatively charged SLB and various peptides by measuring the fluorescence signal[31,32]. Beyond this, the supercritical angle technique was recently applied to Raman spectroscopy[33]. Briefly, classical Raman spectroscopy is a label-free technique that detects the inelastic scattering of incident monochromatic photons upon excitation of the sample[34,35]. Quantum vibrational energy exchange between the photons and the sample induces vibrational excitation of the studied molecule. When these vibrations within the bounds of the molecule yield a change in polarizability, a Raman signal is observed. From this signal, information about the molecular bonds inside the sample can be extracted. When applied to the study of proteins or polypeptides, the analysis of specific peaks in the Raman spectra allow characterization of the secondary structures that are present in the molecular conformation[36]. Because Aβ is a polypeptide chain of approximately 40 amino acids, such secondary structures are close to the general conformation of the molecule despite the lack of defined tertiary structure. However, inelastic Raman scattering is a rare event because of the typical small Raman cross-sections[37]. Approximately one photon out of 10^{10} is scattered inelastically. In addition, a high concentration of protein or peptide (10–100 mg/mL) is often required to measure spontaneous Raman scattering. Techniques are known to overcome these disadvantages, such as surface-enhanced Raman spectroscopy (SERS). In SERS, the incident photons interacts with noble metal nanostructures, leading to a local increase of the electromagnetic field near the nanostructure[38]. This local increase of the electromagnetic field is called localized surface plasmon resonance (LSPR). A molecule situated near such a LSPR can yield a 10^7–10^8-fold enhanced signal upon interaction with the electromagnetic wave[39]. The combination of supercritical/undercritical angle detection scheme with Raman spectroscopy provides unique information about the spatial location of the chemical groups because of the simultaneous collection of interfacial and bulk sample signals. This feature suggests the great potential of the supercritical angle technique as a characterization technique.

MATERIAL AND METHODS

Setup design and measurements

A custom-made microscope objective was used to collect the near-field and far-field Raman signal that arises from angles that are higher and lower than the critical angle, respectively, and they are hereafter referred to as supercritical angle Raman (SAR) and undercritical angle Raman (UAR), respectively. For a glass–water refractive index discontinuity, this critical angle is 61°, based on the formula $\theta c = \arcsin(n_{water}/n_{glass})$[40]. Therefore, the objective is designed with an internal parabolic-shaped lens that is able to collect radiation from above θc for an aqueous sample or a solution with the same refractive index as water (n = ~1.33). Undercritical light is transmitted through a collection of lenses with a numerical aperture equal to 1.0, which is also used to focus the excitation light (see Supporting Information S1). The custom-made objective is mounted on an inverted Olympus IX71 (Olympus Europa GmbH, Hamburg, Germany). A power tunable diode laser emitting at 633 nm (TOPTICA iBeam Smart; TOPTICA Photonics AG, Munich, Germany) was used as an excitation light source. Optical parts are assembled to drive the collected SAR/UAR signal simultaneously as two concentric collimated beams. They are separated through a 45° mirror toward two identical single-photon avalanche diodes (SPADs). The separated signals could otherwise be injected into a multimode fiber toward a −70°C-cooled charge-coupled device (CCD) camera. The splitting between two detectors allows comparison between the signals mentioned before. See Verders et al. and Serano et al. for a detailed description of the optical setup[30,33]. The Raman signal was recorded using a power of ~50 mW, with an acquisition time of 15 s and accumulation over ten spectra. Each experiment was realized in triplicate and Raman signal measured at (22 ± 1) °C. Blank baseline subtraction and deconvolution of the amide I signal into Gaussian peaks were performed with Origin software (OriginLab, Northampton, Massachusetts, USA).

Lipids and peptides handling

1,2-Dioleoyl-sn-glycero-3-phosphocholine (DOPC) and 1,2-dioleoyl-sn-glycero-3-phospho-L-serine (DOPS) in chloroform were used as received (Avanti Polar Lipids, Alabaster, Alabama, USA). Fluorescently labelled 1,2-dioleoyl-sn-glycero-3-phosphoethanolamine powder (DOPE-Atto647; Atto-tec GmbH, Siegen, Germany) was diluted in chloroform. A mixture of 65% DOPC:35% DOPS was the ratio that was selected for all SLB. When experiments required fluorescent SLB, DOPE-Atto647 was added to the lipid mixture to achieve a mass ratio of 1/62500. This amount was determined to give an optimum fluorescence signal using the supercritical angle fluorescence (SAF) technique. The following protocol was used for both fluorescent and non-fluorescent SLB. The lipid solution was stirred under nitrogen then left under a vacuum (10 mbar) overnight to remove any trace of solvent. Dried lipids were resuspended in degassed "membrane buffer" (NaCl (100 mM), $CaCl_2 \cdot 3H_2O$ (5 mM), Tris (10 mM), pH 7.4; Sigma Aldrich, Buchs, Switzerland) and extruded at least 20 times through a porous membrane (0.1 µm pore size) to yield unilamellar vesicles with a homogeneous size distribution. The vesicle solution was then diluted in the membrane buffer to a concentration of 1 mg/mL. A glass coverslip was glued onto a metal plate after cleaning (cycle of Deconex11, ethanol and Milli-Q water in ultrasonic bath) and O2 plasma treatment was used to make the coverslip surface more hydrophilic. Then, 50 µL of the lipid solution were poured into the sample plate well. When the lipid vesicles that were adsorbed on this coverslip reached a critical concentration, the vesicles fused to form a SLB. Non-disrupted vesicles were removed by extensive washing with the membrane buffer. Finally, SLB was left to stabilize for at least 1 hour with PBS (Sigma Aldrich) before any measurement.

Monomeric Aβ(1–40) and Aβ(1–42) (Rockland, Pennsylvania, USA) powders featured a purity greater than 95%, according to the HPLC data of the supplier. Peptides were reconstituted in a 1% NH4OH solution, then immediately diluted in PBS. The solution was centrifuged at 12,000 rpm for 10 min and any undissolved material was removed. Peptides were aliquoted at a concentration of 1 mg/mL and stored at −20°C until use. For measurement of the peptide Raman signal, 0.05 mg of Aβ dissolved in 50 µL PBS was pipetted onto the SLB. Because the collection of Raman signal and especially SAR

requires a high concentration of peptides, the sample solution had an initial peptide concentration of 0.1% (m/v) and was left to evaporate while recording constantly until the amide I region (1640–1690 cm−1) was visible. This evaporation procedure was not performed during the SERS measurements. The total amount of peptides in each experiment was 0.1 mg with a lipid : peptide molar ratio of 5.5×10^{-3} and an initial peptide concentration of 0.1 % (m/v).

Silicon nanofilaments embedded with gold nanoparticles

Silicon nanofilament (SNF) coating was deposited via chemical vapor deposition (CVD) onto glass slides and functionalized following the protocol of Chiang et al[41]. The substrate was then treated with an oxygen plasma for 5 min at 100 W to become superhydrophilic. Before synthesizing gold nanoparticles, all glassware and stir bars were first cleaned with aqua regia solution (HCl/HNO_3, volume ratio of 3:1) to make sure that no metal ions remained and then they were washed with deionized water. The gold nanoparticles (AuNPs) were synthesized using a modified Turkevich method. First, 0.5 wt% $HAuCl_4$, 1 wt% trisodium citrate, and 0.1 wt% $AgNO_3$ were prepared in aqueous solutions and these three solutions were stored at 4°C. Subsequently, a solution was prepared by mixing 85 µL $AgNO_3$ and 2 mL HAuCl4, and then various amounts of trisodium citrate aqueous solution (0.4 mL or 3 mL) were added to the solution, respectively. This solution was further diluted with deionized water to a total volume of 5 mL. The prepared slides were placed into a reaction container with 95 mL deionized water. The prepared solution was injected into the container until the water began to boil. The solution color turned from light yellow to purple to ruby red. Various sizes of AuNPs were obtained after the 1-hour reaction, depending on the trisodium citrate solution volume that was added.

RESULTS AND DISCUSSION

Characterization of lipids

In the first step, fluorescence imaging was performed to assess the successful formation of the SLB, before recording the Raman signal (see Supporting Information S2). Subsequently, Raman measurements have been executed with fluorescent DOPE-free SLBs. Although the formation of the bilayer could be confirmed, the current system could not collect the Raman scattering from a unilamellar bilayer with SAR or with UAR (Figure 1.a). The SLB had a thickness of about 4.93 nm[42], which led to dominance of the supernatant water molecule background in the Raman signal despite their intrinsically low Raman cross-section scattering. The interfacial selectivity of the supercritical angle system prevented dominance of the water band at 3300 cm^{-1}, but the characteristic peaks of the lipid molecules were still not visible. As mentioned previously, the SLB thickness limited the number of available photons that were scattered from lipids. In addition, classical Raman technique has a low sensitivity. This disadvantage was confirmed in other reports, and therefore the study of such a membrane model via Raman spectroscopy is usually achieved

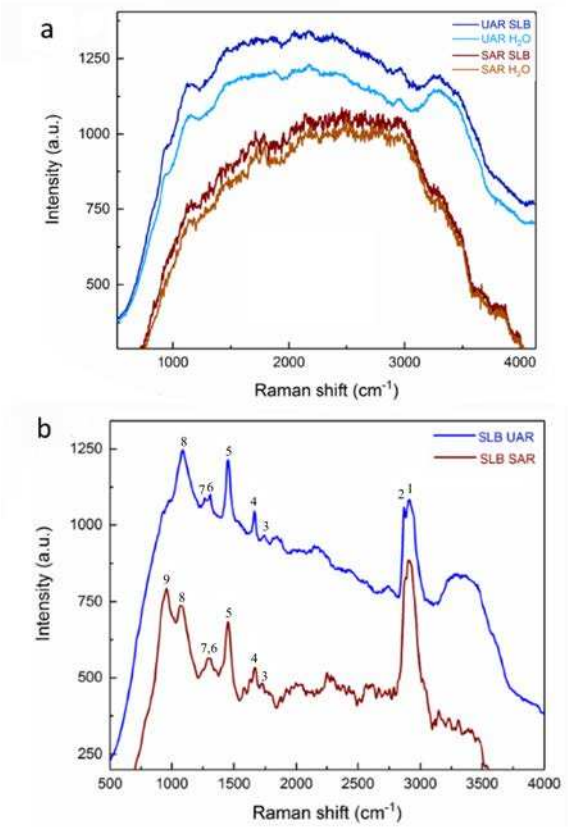

Figure 1. (a) SAR/UAR spectra of non-fluorescent SLB compared with pure water, (b) SAR/UAR spectra of multilamellar lipid structure/vesicles with a minute amount of DOPE-Atto647. See Table 1 for peak assignment.

Table 1. Raman shifts and assignments in Fig. 1

Wavenumber (cm^{-1})	Assignment
2902 (1)	CH_2 fermi resonance
2872 (2)	CH_2 sym. stretching
1742 (3)	C=O stretching
1665 (4)	C=C
1451 (5)	CH_2 scissoring
1309 (6)	CH_2 twisting
1265 (7)	=C-H in plane
1084 (8)	C-C stretching
958 (SAR) (9)	O-P-O sym. stretching

using enhancement techniques[43–45]. From our result, we concluded that the signal of unilamellar SLB is not detected using classical Raman spectra. The Raman spectra of peptides would not be broadened by SLB scattering if both species are present in the sample, and only the interactions with the SLB would influence the peptide signal. This might be an advantage to specifically observe the Aβ signal upon adsorption on a lipid bilayer. However, to confirm that the absence of the lipid signal was caused by an insufficient amount of lipid molecules, further measurements were reproduced while targeting multilamellar bilayers or undisrupted vesicles. Omission of the extrusion process described in the lipid handling section yield-

ed the stacking of the vesicles in these lipid structures. For this experiment, the use of a minute amount of fluorescent DOPE allowed specific targeting of these stacking areas by fluorescent mapping of the sample (Supporting Information S2). The collected Raman spectra (Figure 1.b) displayed a fluorescence band component, but the peaks protruding from the fluorescence baseline allowed characterization of the lipids and proved this method to overcome the poor signal-to-noise issue encountered with unilamellar SLB. Assignment of the peaks is reported in Table 1 [46]. One sharp peak that was specific to the SAR spectrum and interfacial region was situated at 958 cm^{-1}, and it corresponded to O-P-O symmetric stretching[47]. The intensity of this peak might be caused by the packing of the lipid polar head near the substrate. In conclusion, it was shown that unilamellar SLB was not detected with classical Raman spectroscopy because of a lack of photon scattering from the lipids. However, an increase of the amount of lipids within the detection volume by applying multilamellar layers led to the detection of scattered photons without using any enhancement techniques.

Characterization of adsorbed Aβ secondary structure

In this work, the scattered Raman signal was recorded for both Aβ(1–40) and Aβ(1–42) adsorbed on unilamellar SLB composed of 65% DOPC and 35% DOPS (without fluorescent DOPE). Since the membrane curvature has been showed to influence and be influenced by Aβ aggregation, the lipid composition is a matter of importance. Significant membrane curvature accelerates fibril growth, while flat bilayers exhibit a more homogeneous alkyl chains core and trap the peptides before seed formation[48]. DOPE was reported to increase the membrane curvature but was not used because of the undesired fluorescent background. While DOPS is normally concentrated in the inner leaflet of the bilayer, both DOPS and DOPC molecules exhibit rather cylindrical shape[49]. This feature combined with the properties of a homogeneous SLB suggested a low curvature of bilayer used in the following experiments. The same area of the sample was targeted to collect undercritical angle and supercritical angle scattered Raman data (UAR/SAR) (see Supporting Information S3). An exhaustive analysis of Aβ peaks has been realized by Dong et al[50]. However, the analysis of the amide I peak is the first step toward the elucidation of Aβ secondary structures. As previously mentioned, this spectral region is located between ~1640 and 1690 cm^{-1} and primarily represents the C=O stretching of the amide bonds. Some discrepancies were found in the literature about the frequency of the Raman signal that is associated with secondary structures[36,51–53]. For the most part, references in literature define an amide I peak at 1650 ± 10 cm^{-1} as typical of α-helix structures, while a peak around 1670 ± 10 cm^{-1} denotes the presence of β-sheet structures. Some authors attribute a value between 1660 and 1670 cm^{-1} to a disordered secondary structure. The amide I signal was deconvoluted into Gaussian peaks and assigned based on the above-mentioned references. Aβ(1–42) spectra in the UAR and SAR channels exhibited some discrepancies. First, the UAR intensity was higher than SAR. It was easily explained by the larger collection volume of the UAR technique. In addition, the areas of the deconvoluted peaks and their ratios in the two spectra were different. Small shifts in the wavenumbers of analogous deconvoluted peaks were also observed between the UAR and

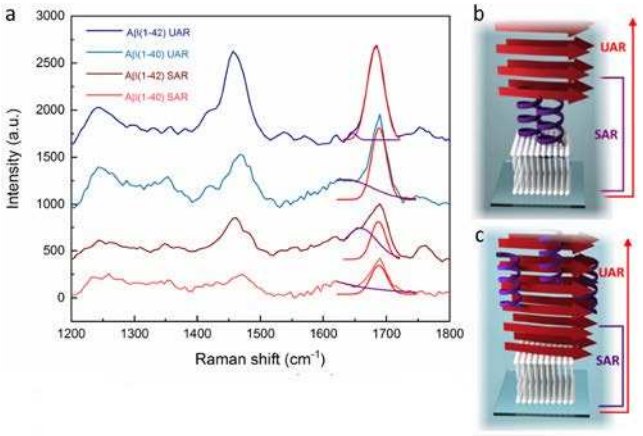

Figure 2. (a) Amide I and III regions of SAR and UAR spectra of Aβ incubated on SLB after partial evaporation of the buffer (27-30 h). Amide I is deconvoluted into α-helix (purple) and β-sheet peaks. (b) Scheme of the hypothetical structure of Aβ(1–42) that is adsorbed onto SLB. (c) Scheme of the hypothetical structure of Aβ(1–40) adsorbed onto SLB.

SAR spectra. These variations showed that the structure of Aβ was influenced by its proximity with the SLB. The SAR amide I of Aβ(1–42) was deconvoluted into two peaks whose maxima were at 1660 and 1689 cm^{-1} respectively (purple and red peaks in Figure 2.a). The former shift value corresponded to a structure between an α-helix and a disordered structure, while the latter was attributed to a β-sheet structure blue-shifted towards higher vibration frequencies. Both secondary structures appeared in the supercritical angle emitting region, near the interface. However, the β-sheet peak area only represents 46.9% of the α-helix peak area, dominant in SAR. In the UAR spectrum, the amide I was also deconvoluted into two peaks situated at 1648 and 1683 cm^{-1}, attributed to α-helix and β-sheet. In the UAR spectrum, the area of the peak attributed to α-helix was only 3% of the β-sheet peak area and hardly distinguishable from the baseline. Further evidence of the predominance of β-sheet in UAR was found in the amide III region where the β-sheet peak at 1242 cm^{-1} protruded from the baseline. This evidence of reversed dominant structure exhibited by the peptide in UAR and SAR showed a tendency towards the α-helix structure when the peptide was close to the lipid media. This hypothesis is in agreement with other research where the α-helix structure featured an enhanced stability in organic solvent or other low polarity media[15,54,55]. According to these results, the charged residues of Aβ are more homogeneously distributed in the α-helix conformation of the molecule, preventing dipole formation. This apolar structure renders its insertion into a hydrophobic core, such as a lipid bilayer, more favorable. Conversely, Aβ seems prone to adopt a random coil structure in aqueous media, or to fold as a β-sheet when a critical concentration is reached. This was confirmed by the large predominance of the β-sheet peaks in the UAR spectrum, where most of the scattered light comes from the volume above the interfacial SLB. The most interesting interpretation of these results is that both secondary structures coexisted simultaneously in the same area of the sample and were differentiated by their axial distance from the lipids. This adds details to the common hypothesis about the fibrillation process where the structure of adsorbed Aβ is converted into the fibril macrostructure (β-sheet stack)[15,56–58]. A mixture of α-helix and β-sheet structures was also observed by Sahoo et al.

in Aβ interacting with polymer encased lipid-nanodiscs[59]. In their work, slightly acidic pH conditions and a lower peptide-to-lipids molar ratio promoted an initial folding into helices, followed by a transition toward β-sheets. Our data presented here in Figure 2.b suggest that the helical secondary structure adopted by Aβ remained as an "anchor-like" part even after the aggregation of additional peptides into another structure.

Raman spectra of Aβ(1–40) were also recorded after SLB adsorption and analyzed (Figure 2.a). The localization of the secondary structures in UAR and SAR was different between the two types of peptides. In contrast to Aβ(1–42), the β-sheet peak of Aβ(1–40) at 1687 cm^{-1} was dominant in both SAR and UAR. The amide III peak at 1243 cm^{-1} also assessed the presence of β-sheets in the bulk solution. In the UAR spectrum, the left part of the amide I peak was deconvoluted into a broad peak at 1640 cm^{-1}, which could be attributed to the scattering of the α-helix structure. Broadening was interpreted as structural variations with different vibrational scattering. These structural variations could be the progressive transitions from unstable α-helix toward random coil or β-sheet. In SAR, besides the β-sheet peak at 1687 cm^{-1}, the deconvoluted amide I yielded a peak at 1624 cm^{-1}. However, the latter was too red-shifted and affected by the baseline noise to be attributed to the α-helix. Therefore, transient α-helix structure was assumed in the UAR channel only, far from the SLB. This is in contradiction with the results of Aβ(1–42) and with the usual hypothesis of Aβ aggregation. It is hypothesized that Aβ(1–40) folded into α-helix upon interaction with the lipids might have desorbed and are no longer concentrated near the bilayer. This greater tendency of Aβ(1–40) to desorb from the membrane was observed previously and explained by a weaker insertion within the bilayer[60]. Desorbed Aβ with the α-helix structure could interact with the peptides in the bulk solution (UAR), which exhibit β-sheet conformations (Figure 2.c). Unfolding and transition of the helical structure toward β-sheet might occur when the peptide is not inserted in an apolar medium anymore.

Surface-enhanced Raman spectroscopy of amyloid-β

The use of plasmonic resonance produced by silver or gold nanoparticles on vibrational light scattering is widely used and is known as SERS. Various methods are available to generate the metal plasmon resonance near the sample. In the present work, SNFs functionalized with gold nanoparticles were synthesized from trichloromethylsilane (TCMS) and used as a substrate for the formation of SLB. The formation of SLB was first assessed by fluorescence control with labelled DOPE before performing the Raman experiments without DOPE. Successful SLB formation was confirmed and the Raman spectra of SLB formed on nanofilaments without gold nanoparticles and on bare glass were identical (see Supporting Information S4). However, the presence of gold nanoparticles affected the Raman scattering of the lipids. The UAR spectrum of SLB formed on gold-functionalized SNFs exhibited sharp peaks, characteristic of lipids. Those peaks coming specifically from the vibration of the lipids are detailed in Table 2. However, two intense peaks at 1566 cm^{-1} and 1330 cm^{-1} were observed. These two peaks came from the gold substrate or nanoparticles (see Supporting Information S5) resulted from the photoluminescence effect of the metal[61].

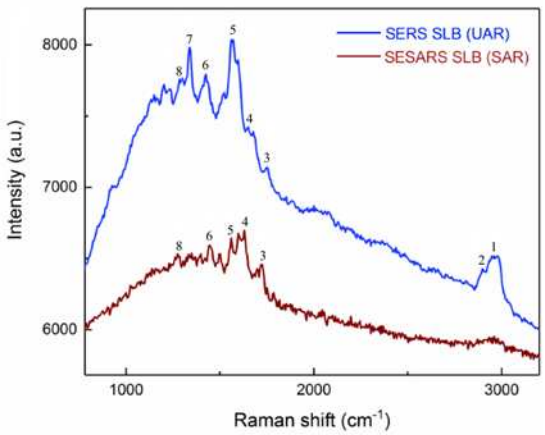

Figure 3. Surface-enhanced SAR and UAR spectra of SLB formed on functionalized SNFs. See Table 2 for peak assignment.

Table 2. Raman shifts and assignments in Fig. 3

Wavenumber (cm^{-1})	Assignment
2947 (1)	CH_3 asym. stretching
2895 (2)	CH_2 asym. stretching
1750 / 1725 (SAR) (3)	C=O stretching
1651 / 1635 (SAR) (4)	C=C
1560 (5)	Gold photoluminescence
1448 (6)	CH_2 scissoring
1339 (7)	Gold photoluminescence
1274 (8)	=C-H in plane

The photoluminescence arises from an amplification of the electric field close to the metal (up to ~10 nm away from the surface plasmon). Despite the photoluminescence effect, the SNFs functionalized with gold nanoparticles used for SERS (i.e. UAR) and its supercritical angle equivalent (SESARS) allowed the detection of photons scattered by a single supported bilayer (Figure 3.b). Both the C=O and C=C stretching peaks exhibited a red-shift toward smaller wavenumbers in SAR. This is associated with a lower frequency of vibration, which may be the consequence of the gold nanoparticles that have an impact on the vibrations of the lipid chemical bonds. Indeed, the interaction of gold nanoparticles with lipid bilayers has been reported to increase the ordering of the lipid phase[62], which in turn is expected to yield a decrease of the frequency of vibration[63]. This experiment showed that the detection of a unilamellar-supported lipid bilayer was possible using the SERS technique, and it could be applied to the supercritical angle collection of photons.

The SLB was incubated with an aliquot of Aβ(1–42) (0.22 mM, 0.1% (w/v)) and the Raman signal was collected. The plasmonic surface-enhancement allowed the direct detection of the peptide signal, without the need to evaporate the solvent. The SESARS spectrum after incubation with Aβ is shown in Figure 4. An intense peak at 1651 cm^{-1} (purple arrow) was correlated to the α-helix secondary structure, appearing after incubation with the peptide. The same structure was confirmed by the peak protruding at 1266 cm^{-1} (purple arrow).

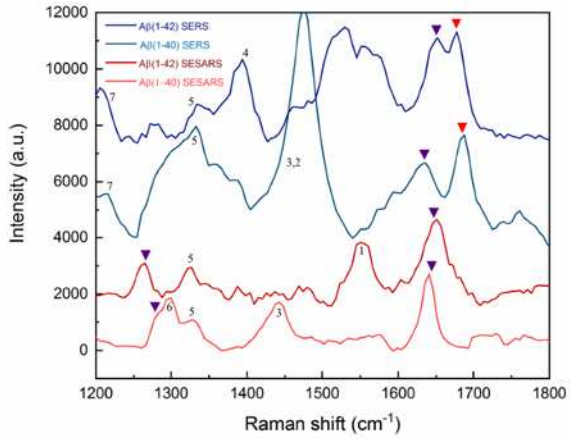

Figure 4. Surface-enhanced SAR (SESARS) and UAR (SERS) spectra of SLB after incubation with 0.22 mM Aβ. Peaks of the secondary structures of the peptide are indicated by purple (α-helix) and red (β-sheet) arrows. See Table 3 for peak assignment.

Table 3. Raman shifts and assignments in Fig. 4

Wavenumber (cm^{-1})	Assignment
1561 (1)	Gold photoluminescence, imidazole (His)
1470 (2)	CH_3 deformation
1442 (3)	CH_2 scissoring
1394 (4)	Gold photoluminescence
1327 (5)	Histidine ring
1300 (6)	CH_2 twisting
1210 (7)	Tyr, Phe

The peak at 1561 cm^{-1} (1) was detected before incubation, but it was broadened with the C=C signal and attributed to photoluminescence. However, its intensity increased drastically after incubation with the peptide. Hetero rings were a plausible source for this increase because of the three histidine residues of each Aβ (His_6, His_{13}, and His_{14}). Thus, the peaks at 1561 cm^{-1} (1) and 1327 cm^{-1} (2) (the latter was not visible before incubation with the peptide) were attributed to a neutral imidazole side chain by Ashikawa et al.[64]. In addition to the appearance of the peptide peaks, a disappearance of the SLB peaks at 1448 cm^{-1}, 1630 cm^{-1}, and 1725 cm^{-1} was observed. This effect was thought to result from either overlapping with the peptide signals or removal of the lipid molecules from the surface. The SERS (UAR) spectrum is displayed in Figure 4. The amide I and amide III peaks appeared only after incubation with the peptide. The peak at 1651 cm^{-1} (purple arrow) was identified as α-helix, but the peak at 1677 cm^{-1} was typical of β-sheet structure. Some other features were observable when comparing the UAR spectra before and after incubation with the peptides. The broad peaks at 1571–1630 cm^{-1} seemed red-shifted to 1540–1600 cm^{-1} as if the corresponding chemical moieties were subjected to a lower vibration frequency. In addition, the characteristic peaks of lipids at 1750 and 1448 cm^{-1} were not visible after incubation with Aβ(1–42). These results confirmed the hypothesis of the previous section about the structure adopted by Aβ(1–42) upon adsorption on the bilayer (Figure 2.b), but it did not require solvent evaporation. This important feature improved the validity of the structure model described before. Unfortunately, little information about the structure of the lipid molecules could be extracted from this experiment, because their signal disappeared after incubation with the peptides.

Incubation of SLB with peptides and characterization by surface-enhanced Raman was repeated with Aβ(1–40). The SESARS and SERS spectra after incubation with the peptide are displayed in Figure 4. The two main differences with control SLB were the apparition of an intense α-helix peak at 1640 cm^{-1} (purple) and a group of peaks around 1300 cm^{-1}. An amide III peak at 1278 cm^{-1} confirmed presence of α-helix structures. The peaks at 1300 (4) and 1327 (2) cm^{-1} were attributed to the C-terminal methylene twisting vibration and imidazole, respectively. In the SERS spectrum, the carbonyl peak of the SLB at 1730 cm^{-1} was not visible after incubation with Aβ. The amide III region was too broadened for accurate characterization, hence the amide I region was used instead to determine the structure of the peptides. Two peaks were detected, corresponding to both α-helix (purple) and β-sheet (red) secondary structures. This result was identical to the structures observed for Aβ(1–42), indicating a preferential folding into helices near the membrane, with a concentration of β-sheets above the surface of the SLB. However, this contrasts with the structure hypothesized using classical Raman spectroscopy. No α-helices were observed near the SLB and only a small fraction of their Raman scattering was detected above the bilayer. A possible explanation for this apparent inconsistency is that results obtained with classical Raman required a high local concentration of peptides, which is a trigger for the folding of Aβ into β-sheet and their stacking. The increased sensitivity of SERS allows the data to be recorded at lower concentration, before a conformational transition. SERS data recorded after the evaporation of the buffer confirmed this hypothesis: the β-sheet peak became dominant in both spectra (see Supporting Information S6), yielding results similar to normal Raman spectroscopy.

CONCLUSION

Raman spectroscopy is a powerful characterization technique that allows determination of the covalent bonds within a molecule by vibrational spectroscopy. Applied to biomolecules like proteins and polypeptides, it allows the identification of the local conformation or secondary structure of the sample. Here, Raman spectroscopy was combined with surface-sensitive supercritical angle technique to monitor and characterize a bio-mimicking system of Alzheimer disease. The system was composed of a lipid supporter bilayer (SLB) and Aβ peptides. Raman measurements comprised a traditional undercritical angle (UAR) and a surface-selective supercritical angle (SAR) signal collection. Multilamellar patches or non-disrupted vesicles were required to detect the Raman scattering of the lipids. The spectra of the lipids were almost identical for both UAR and SAR, except for the lipid phosphate headgroup located near the interface and only visible with SAR. We also collected the Raman spectra of Aβ peptides adsorbed onto a standard unilamellar SLB. Comparison between UAR and SAR revealed two secondary structures present simultaneously in Aβ aggregates. The location of the two structures was dependent on their proximity with the lipid bilayer. Aβ(1–42) located close to the lipid surface exhibited a dominant α-helix structure while the peptides aggregated further away from the membrane adopted a β-sheet structure. Aβ(1–40) also exhibit-

ed the two structures, but the α-helices were no longer specific to the surface. Its presence comparably far from the membrane suggested that helical peptides might have desorbed from the SLB. The structure of the lipids and Aβ peptides was also investigated with SERS by formation of the SLB on a layer of gold-embedded SNFs. The SERS experiment confirmed with a lower concentration of peptides the conformation observed previously with classical Raman spectroscopy. This result was an example of how the selectivity between UAR and SAR could provide advantages when combined, even with an intrinsic surface-enhancement technique. The UAR (i.e. SERS) spectrum alone would only permit detection of both the α-helix and β-sheet without any information about their localization. However, the presence of only one specific structure in Surface-enhanced SAR (SESARS) demonstrated that one structure was situated near the SLB surface. Conversely, SAR spectroscopy alone would not allow the detection of both structures. Discrepancies between the structures observed with classical and enhanced Raman were correlated to the peptide concentration. Our data suggested that both Aβ variants folded into the α-helix during initial adsorption onto the membrane (i.e. with a lower local concentration of peptide). Peptides non adsorbed or desorbed from the SLB might undergo a transition toward β-sheet at high concentrations. However, physiological interpretation must be made carefully because of the high peptide concentration, even in surface-enhanced Raman.

ASSOCIATED CONTENT

Supporting Information

S1. Scheme of the microscope objective.
S2. Fluorescent imaging of the SLB.
S3. SAR/UAR Spectra of Aβ and peak assignment.
S4. Scheme of the SERS substrate and SLB spectra.
S5. SERS spectra of SLB on different gold substrates.
S6. SERS of Aβ(1–40) on SLB after buffer evaporation.

AUTHOR INFORMATION

Corresponding Author

Stefan Seeger: sseeger@chem.uzh.ch

Author Contributions

V. Dubois and D. Serrano conducted and optimized technical aspects of this work. X. Zhang developed the SERS substrates used in this work. V. Dubois and S. Seeger conducted experimental design, data analysis and interpretation. V. Dubois and S. Seeger wrote/edited the manuscript.

ACKNOWLEDGMENT

This work was supported by the University of Zürich.

REFERENCES

(1) Dinner, A. R., Šali, A., Smith, L. J., Dobson, C. M., and Karplus, M. Understanding protein folding via free-energy surfaces from theory and experiment, Trends in Biochemical Sciences 25 **2000**, 331–339.

(2) Dobson, C. M. Protein folding and misfolding, Nature 426 **2003**, 884–890.

(3) Clark, P. L. Protein folding in the cell. Reshaping the folding funnel, Trends in Biochemical Sciences 29 **2004**, 527–534.

(4) Dobson, C. M. The structural basis of protein folding and its links with human disease, Philosophical transactions of the Royal Society of London. Series B, Biological sciences 356 **2001**, 133–145.

(5) Thomas, P. J., Qu, B.-H., and Pedersen, P. L. Defective protein folding as a basis of human disease, Trends in Biochemical Sciences 20 **1995**, 456–459.

(6) Karran, E., Mercken, M., and Strooper, B. de. The amyloid cascade hypothesis for Alzheimer's disease: an appraisal for the development of therapeutics, Nature reviews. Drug discovery 10 **2011**, 698–712.

(7) Masters, C. L., Simms, G., Weinman, N. A., Multhaup, G., McDonald, B. L., and Beyreuther, K. Amyloid plaque core protein in Alzheimer disease and Down syndrome, Proceedings of the National Academy of Sciences 82 **1985**, 4245–4249.

(8) D. F. Clayton, J. M. George. The synucleins: a family of proteins involved in synaptic function, plasticity, neurodegeneration and disease, Trends Neurosci. 21 **1998**, 249–254.

(9) Lashuel, H. A., Overk, C. R., Oueslati, A., and Masliah, E. The many faces of α-synuclein. From structure and toxicity to therapeutic target, Nature reviews. Neuroscience 14 **2013**, 38–48.

(10) Payton, J. E., Perrin, R. J., Clayton, D. F., and George, J. M. Protein–protein interactions of alpha-synuclein in brain homogenates and transfected cells, Molecular Brain Research 95 **2001**, 138–145.

(11) Mukherjee, A., Morales-Scheihing, D., Butler, P. C., and Soto, C. Type 2 diabetes as a protein misfolding disease, Trends in molecular medicine 21 **2015**, 439–449.

(12) Muresan, V., and Ladescu Muresan, Z. Amyloid-beta precursor protein. Multiple fragments, numerous transport routes and mechanisms, Experimental cell research 334 **2015**, 45–53.

(13) O'Brien, R. J., and Wong, P. C. Amyloid precursor protein processing and Alzheimer's disease, Annual review of neuroscience 34 **2011**, 185–204.

(14) Lee, J. P., Stimson, E. R., Ghilardi, J. R., Mantyh, P. W., Lu, Y.-A., Felix, A. M., Llanos, W., Behbin, A., and Cummings, M. 1H NMR of A.beta. Amyloid Peptide Congeners in Water Solution. Conformational Changes Correlate with Plaque Competence, Biochemistry 34 **1995**, 5191–5200.

(15) Tomaselli, S., Esposito, V., Vangone, P., van Nuland, N. A. J., Bonvin, A. M. J. J., Guerrini, R., Tancredi, T., Temussi, P. A., and Picone, D. The alpha-to-beta conformational transition of Alzheimer's Abeta-(1-42) peptide in aqueous media is reversible. A step by step conformational analysis suggests the location of beta conformation seeding, Chembiochem : a European journal of chemical biology 7 **2006**, 257–267.

(16) Giacomelli, C. E., and Norde, W. Conformational changes of the amyloid beta-peptide (1-40) adsorbed on solid surfaces, Macromolecular bioscience 5 **2005**, 401–407.

(17) Jahn, T. R., Makin, O. S., Morris, K. L., Marshall, K. E., Tian, P., Sikorski, P., and Serpell, L. C. The common architecture of cross-beta amyloid, Journal of molecular biology 395 **2010**, 717–727.

(18) Peter T. Lansbury, JR. Evolution of amyloid: What normal protein folding may tell us about fibrillogenesis and disease, Proc. Natl. Acad. Sci. USA 96 **1999**, 3342–3344.

(19) Ian V. J. Murray, Michael E. Sindoni, and Paul H. Axelsen Promotion of Oxidative Lipid Membrane Damage by Amyloid β Proteins, Biochemistry 44 **2005**, 12606–12613.

(20) Smith, D. G., Cappai, R., and Barnham, K. J. The redox chemistry of the Alzheimer's disease amyloid beta peptide, Biochimica et biophysica acta **2007**, 1976–1990.

(21) Sasahara, K., Morigaki, K., and Shinya, K. Effects of membrane interaction and aggregation of amyloid β-peptide on lipid mobility and membrane domain structure, Physical chemistry chemical physics 15 **2013**, 8929–8939.

(22) Caughey, B., and Lansbury, P. T. Protofibrils, pores, fibrils, and neurodegeneration. Separating the responsible protein aggregates from the innocent bystanders, Annual review of neuroscience 26 **2003**, 267–298.

(23) M. Kawahara,N. Arispe, Y. Kuroda, and E. Rojas. Alzheimer's Disease Amyloid (8-Protein Forms Zn2+ Sensitive, Cation-Selective Channels Across Excised Membrane Patches from Hypothalamic Neurons, Biophysical journal 73 **1997**, 67–75.

(24) Sciacca, Michele F M, Kotler, S. A., Brender, J. R., Chen, J., Lee, D.-k., and Ramamoorthy, A. Two-step mechanism of membrane

disruption by Aβ through membrane fragmentation and pore formation, Biophysical journal 103 **2012**, 702–710.

(25) Khan, M. S., Dosoky, N. S., and Williams, J. D. Engineering lipid bilayer membranes for protein studies, International journal of molecular sciences 14 **2013**, 21561–21597.

(26) Czogalla, A., Grzybek, M., Jones, W., and Coskun, U. Validity and applicability of membrane model systems for studying interactions of peripheral membrane proteins with lipids, Biochimica et biophysica acta **2014**, 1049–1059.

(27) Richter, R. P., Berat, R., and Brisson, A. R. Formation of solid-supported lipid bilayers. An integrated view, Langmuir : the ACS journal of surfaces and colloids 22 **2006**, 3497–3505.

(28) J. Enderlein, T. Ruckstuhl, and S. Seeger. Highly efficient optical detection of surface-generated fluorescence, Appl. Opt. 38 **1999**, 724–732.

(29) T. Ruckstuhl, D. Verdes. Supercritical angle fluorescence (SAF) microscopy, Optic express 12 **2004**, 4246–4254.

(30) D. Verdes, T. Ruckstuhl, S. Seeger. Parallel two-channel near- and far-field fluorescence microscopy, J. Biomed. Opt. 12(3) **2007**.

(31) Rabe, M., Soragni, A., Reynolds, N. P., Verdes, D., Liverani, E., Riek, R., and Seeger, S. On-surface aggregation of α-synuclein at nanomolar concentrations results in two distinct growth mechanisms, ACS chemical neuroscience 4 **2013**, 408–417.

(32) Reynolds, N. P., Soragni, A., Rabe, M., Verdes, D., Liverani, E., Handschin, S., Riek, R., and Seeger, S. Mechanism of membrane interaction and disruption by α-synuclein, Journal of the American Chemical Society 133 **2011**, 19366–19375.

(33) Serrano, D., and Seeger, S. Supercritical angle Raman microscopy. A surface-sensitive nanoscale technique without field enhancement, Light Sci Appl 6 **2017**, e17066.

(34) E. Smith, G. D. Modern Raman Spectroscopy – A Practical Approach, Wiley **2005**.

(35) Long, D. A. The Raman effect. A unified treatment of the theory of Raman scattering by molecules. Wiley **2002**.

(36) Rygula, A., Majzner, K., Marzec, K. M., Kaczor, A., Pilarczyk, M., and Baranska, M. Raman spectroscopy of proteins. A review, J. Raman Spectrosc. 44 **2013**, 1061–1076.

(37) Penney CM, Goldman LM, Lapp M. Raman scattering cross sections., Nat Phys Sci **1972**, 110–112.

(38) Schlücker, S. Surface-enhanced Raman spectroscopy. Concepts and chemical applications, Angewandte Chemie (International ed. in English) 53 **2014**, 4756–4795

(39) Xu, H., Aizpurua, J., Käll, M., and Apell, P. Electromagnetic contributions to single-molecule sensitivity in surface-enhanced Raman scattering, Phys. Rev. E 62 **2000**, 4318–4324.

(40) Winterflood, C. M., Ruckstuhl, T., Verdes, D., and Seeger, S. Nanometer axial resolution by three-dimensional supercritical angle fluorescence microscopy, Physical review letters 105 **2010**, 108103.

(41) Chiang, C.-Y., Liu, T.-Y., Su, Y.-A., Wu, C.-H., Cheng, Y.-W., Cheng, H.-W., and Jeng, R.-J. Au Nanoparticles Immobilized on Honeycomb-Like Polymeric Films for Surface-Enhanced Raman Scattering (SERS) Detection, Polymers 9 **2017**, 93.

(42) Hähl, H., Möller, I., Kiesel, I., Campioni, S., Riek, R., Verdes, D., and Seeger, S. α-Synuclein insertion into supported lipid bilayers as seen by in situ X-ray reflectivity, ACS chemical neuroscience 6 **2015**, 374–379.

(43) Sweetenham, C. S., and Notingher, I. Raman spectroscopy methods for detecting and imaging supported lipid bilayers, Spectroscopy 24 **2010**, 113–117.

(44) Lee, C., and Bain, C. D. Raman spectra of planar supported lipid bilayers, Biochimica et biophysica acta **2005**, 59–71.

(45) Wright, A. J., Richens, J. L., Bramble, J. P., Cathcart, N., Kitaev, V., O'Shea, P., and Hudson, A. J. Surface-enhanced Raman scattering measurement from a lipid bilayer encapsulating a single decahedral nanoparticle mediated by an optical trap, Nanoscale 8 **2016**, 16395–16404.

(46) Czamara, K., Majzner, K., Pacia, M. Z., Kochan, K., Kaczor, A., and Baranska, M. Raman spectroscopy of lipids. A review, J. Raman Spectrosc. 46 **2015**, 4–20.

(47) Frank D. Gunstone, John L. Harwood, Albert J. Dijkstra The Lipid Handbook 3rd Edition **2007**, CRC press, Boca Raton (Florida).

(48) Terakawa, M. S., Lin, Y., Kinoshita, M., Kanemura, S., Itoh, D., Sugiki, T., Okumura, M., Ramamoorthy, A., and Lee, Y.-H. Impact of membrane curvature on amyloid aggregation, Biochimica et biophysica acta. Biomembranes. **2018**.

(49) McMahon, H. T., and Boucrot, E. Membrane curvature at a glance, Journal of cell science 128 **2015**, 1065–1070.

(50) Dong, J., Atwood, C. S., Anderson, V. E., Siedlak, S. L., Smith, M. A., Perry, G., and Carey, P. R. Metal binding and oxidation of amyloid-beta within isolated senile plaque cores: Raman microscopic evidence, Biochemistry 42 **2003**, 2768–2773.

(51) Kurouski, D., Van Duyne, Richard P, and Lednev, I. K. Exploring the structure and formation mechanism of amyloid fibrils by Raman spectroscopy: a review, The Analyst 140 **2015**, 4967–4980.

(52) Maiti, N. C., Apetri, M. M., Zagorski, M. G., Carey, P. R., and Anderson, V. E. Raman spectroscopic characterization of secondary structure in natively unfolded proteins. Alpha-synuclein, Journal of the American Chemical Society 126 **2004**, 2399–2408.

(53) Apetri, M. M., Maiti, N. C., Zagorski, M. G., Carey, P. R., and Anderson, V. E. Secondary structure of alpha-synuclein oligomers. Characterization by raman and atomic force microscopy, Journal of molecular biology 355 **2006**, 63–71.

(54) Ikeda, K., Yamaguchi, T., Fukunaga, S., Hoshino, M., and Matsuzaki, K. Mechanism of amyloid β-protein aggregation mediated by GM1 ganglioside clusters, Biochemistry 50 **2011**, 6433–6440.

(55) Drolle, E., Hane, F., Lee, B., and Leonenko, Z. Atomic force microscopy to study molecular mechanisms of amyloid fibril formation and toxicity in Alzheimer's disease, Drug metabolism reviews 46 **2014**, 207–223.

(56) Matsuzaki, K. Physicochemical interactions of amyloid beta-peptide with lipid bilayers, Biochimica et biophysica acta 1768 **2007**, 1935–1942.

(57) Butterfield, S. M., and Lashuel, H. A. Amyloidogenic protein-membrane interactions: mechanistic insight from model systems, Angewandte Chemie (International ed. in English) 49 **2010**, 5628–5654.

(58) Kotler, S. A., Walsh, P., Brender, J. R., and Ramamoorthy, A. Differences between amyloid-β aggregation in solution and on the membrane: insights into elucidation of the mechanistic details of Alzheimer's disease, Chemical Society reviews 43 **2014**, 6692–6700.

(59) Sahoo, B. R., Genjo, T., Bekier, M., Cox, S. J., Stoddard, A. K., Ivanova, M., Yasuhara, K., Fierke, C. A., Wang, Y., and Ramamoorthy, A. Alzheimer's amyloid-beta intermediates generated using polymer-nanodiscs, Chemical communications (Cambridge, England) 54 **2018**, 12883–12886.

(60) Joseph T. Jarrett, Elizabeth P. Berger, and Peter T. Lansbury, Jr. The Carboxy Terminus of the Amyloid Protein Is Critical for the Seeding of Amyloid Formation: Implications for the Pathogenesis of Alzheimer's Disease, Biochemistry 32 **1993**, 4693–4697.

(61) Ivanov, V. G., Todorov, N. D., Petrov, L. S., Ritacco, T., Giocondo, M., and Vlakhov, E. S. Strong surface enhanced Raman scattering from gold nanoarrays obtained by direct laser writing, J. Phys.: Conf. Ser. 764 **2016**, 12023.

(62) Mhashal, A. R., and Roy, S. Effect of gold nanoparticle on structure and fluidity of lipid membrane, PloS one 9 **2014**, e114152.

(63) Weeraman, C., Yatawara, A. K., Bordenyuk, A. N., and Benderskii, A. V. Effect of nanoscale geometry on molecular conformation: vibrational sum-frequency generation of alkanethiols on gold nanoparticles, Journal of the American Chemical Society 128 **2006**, 14244–14245.

(64) Ashikawa, I., and Itoh, K. Raman spectra of polypeptides containingL-histidine residues and tautomerism of imidazole side chain, Biopolymers 18 **1979**, 1859–187

Authors are required to submit a graphic entry for the Table of Contents (TOC) that, in conjunction with the manuscript title, should give the reader a representative idea of one of the following: A key structure, reaction, equation, concept, or theorem, etc., that is discussed in the manuscript. Consult the journal's Instructions for Authors for TOC graphic specifications.